AUTHOR'S DATABASE ENTRY SHEET

TITLE OF THE NATO MEETING/NATO ASI SERIES VOLUME:

Gravity Wave Processes and Their Parameterization in Global Climate Models

NAME OF THE DIRECTOR: K. Hamilton YEAR: 1997

NAME OF THE EDITORS: K. Hamilton

TITLE OF THE PAPER: Observations of Gravity Waves with the UARS Microwave Limb Sounder

AUTHOR OF THE PAPER: Dong L. Wu

AUTHOR'S AFFILIATIONS:

Mail Stop 183-701, Jet Propulsion Laboratory, California Institute of Technology, 4800 Oak Grove Drive, Pasadena, California 91109, U.S.A.

CO-AUTHOR: Joe W. Waters

KEYWORDS/ ABSTRACTS: gravity wave/ satellite observations/ polar vortex/ deep convection/ surface topography/ mean winds/ temperature variance/ microwave radiance

The Upper Atmosphere Research Satellite Microwave Limb Sounder has observed small- and meso-scale temperature fluctuations with its 63 GHz saturated radiances in 30-80 km altitudes. These fluctuations, showing phase coherence and amplitude growth with height, are likely caused by the gravity waves of vertical wavelengths greater than 10 km. A variance analysis, used to extract the temperature variance from total observed radiance variance, allows us to map gravity wave activity on a global-and-monthly basis. Wave variance maps and climatology are currently obtained for October 1992 - October 1993, showing interesting features associated with stratospheric polar vortices, tropospheric deep convection, and surface topography during winter/summer months, and a predominant annual (semiannual) variation is found in the stratosphere (mesosphere). It is shown that separated analyses for ascending and descending measurements can be used to infer wave propagation directions.

Observations of Gravity Waves with the UARS Microwave Limb Sounder

Dong L. Wu and Joe W. Waters
Mail Stop 183-701, Jet Propulsion Laboratory
California Institute of Technology
4800 Oak Grove Drive
Pasadena, California 91109
U.S.A.

1. Introduction

Geographical and spectral distributions of gravity waves are crucial for large-scale circulation and local mixing in the atmosphere. Lack of global gravity wave (GW) climatology makes it difficulty to quantify the total momentum and energy forcings contributed by the small-scale eddies. Observations of the GW distributions have been provided previously by various techniques such as radar [Meek et al. 1985; Vincent and Fritts 1987; Fukao et al. 1994], lidar [Wilson et al. 1991], balloon [Allen and Vincent 1995], rocket [Hirota 1984], aircraft [Nastrom and Gage 1985] and satellite [Fetzer and Gille 1994]. However, each of these techniques only measures waves of certain spatial and temporal scales. Observations from radar, lidar, balloon and rocket yield good temporal and vertical resolutions usually at one geographical location while aircraft observations provide good horizontal resolution but for a short period of time. It is difficult in general for space-borne sensors to obtain the same resolutions, but observations of GWs at somewhat larger scales are feasible, for example using saturated radiances from the Upper Atmosphere Research Satellite (UARS) Microwave Limb Sounder (MLS) [Wu and Waters 1996].

Observations from UARS MLS can provide geographical distributions and seasonal climatology of small-scale GWs in the middle atmosphere. The gravity waves to which MLS is sensitive are those with relatively long (>10 km) vertical wavelengths and therefore are of importance to the momentum budget in the mesosphere and lower thermosphere. The UARS MLS, in operation since 12 September 1991, was designed to measure profiles of molecular abundances (O_3, ClO, and H_2O), temperature and pressure in the middle atmosphere using thermal emission features near 63, 183 and 205 GHz [Waters 1993; Barath et al. 1993]. We recently made an extraordinary use of the saturated radiances from the 63-GHz radiometer channels, which measure atmospheric temperatures at different altitude layers, for small-scale gravity wave study [Wu and Waters 1996]. This study is benefited from a good global coverage ranging from 34° latitude in one hemisphere to 80° in the other, because the MLS field of view is 90° from the UARS orbital velocity and the orbit is 598 km high with 57° inclination. The UARS makes 10 yaw maneuvers each year allowing alternating views of high latitudes in the two hemispheres with a periodicity of ~36 days. Section 2 provides some examples of MLS raw radiance measurements where gravity waves are evident as coherent patterns among the measurements at different altitudes. In section 3 sampling issues and temperature weighting functions are discussed. Section 4 describes a variance analysis technique for routine MLS limb-scanning observations which is used to map GW activity on a monthly basis. Section 5 discusses the GW variance maps obtained for January and July periods and a climatology for 1992/93. Summary and conclusions are in section 6.

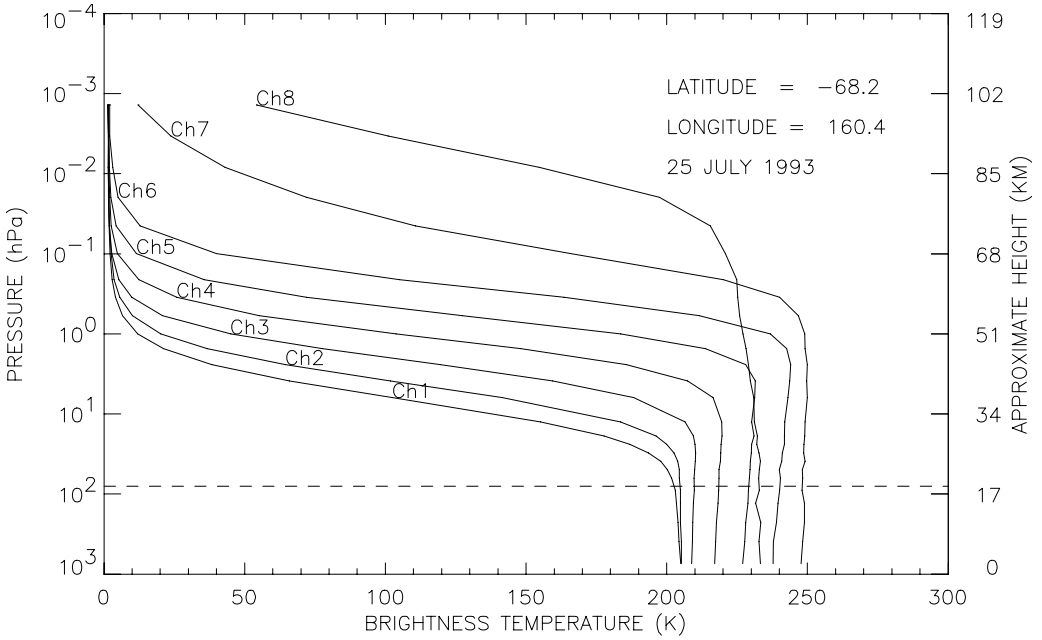

Figure 1. An example of MLS O_2 radiance profiles near 63 GHz as the instrument step-scans from the mesosphere to the surface. Fluctuations in the saturated radiances are generally large for center channels but small for wing channels due to atmospheric temperature variability and instrument noise.

2. MLS 63-GHz Radiance Measurements

Two general scanning mechanisms have been implemented in the MLS operation for atmospheric sampling: limb-scanning and limb-tracking. In routine limb-scanning mode the instrument step-scans the atmospheric limb in ~65 seconds at 2 seconds/step from ~90 km to the surface producing increments of ~5 km in the mesosphere and 1-3 km in the stratosphere and troposphere. Figure 1 shows the radiance profiles of a single scan measured by the 63 GHz radiometer, which resolves an O_2 emission line into 15 spectral channels for retrieving atmospheric tangent pressure and temperature [Fishbein et al. 1996]. All radiances are saturated when the instrument views tangent heights below ~18 km because of strong line absorption. Radiances near line-center (channel 8) saturate at higher altitudes than those near the line-wing (channels 1 and 15 that are symmetric about channel 8). The saturated radiance is a good measure of atmospheric temperature and depends little on the tangent height of pointing. Thus, as the satellite moves along, fluctuations in the saturated radiances actually reflect atmospheric temperature variations in the horizontal direction. Nevertheless, although the radiances below ~18 km are saturated, they still depend weakly and nearly linearly on pointing. By removing this weak linear trend, one can detect fluctuations in the saturated radiances due to horizontal variations in atmospheric temperature.

In limb-tracking mode the instrument tracks the limb, usually at ~18 km tangent height, and makes measurements with the same 2-second sampling frequency as in limb-scanning mode (equivalent to ~15 km horizontal resolution along the suborbital track). Since all 63 GHz channel radiances are optically thick in the 18-km-limb-tracking observation, MLS in this mode measure atmospheric temperature continuously with a good horizontal resolution. Such a data set is quite useful for GW studies. Figure 2 illustrates the sampling pattern for the limb-tracking mode, showing the MLS suborbital tracks on 28 December 1994. As detailed in the inset, the atmosphere is sampled by a series of moving averages with centers separated by ~15 km, while a larger gap in the middle is caused by a 6-second

instrument calibration. The limb-tracking mode was used nearly continuously during 23-30 Dec. 1994, 1 Feb.-20 Mar. and 7-15 Apr. 1995, and normally scheduled for every-third-day operation since then while MLS is on. (Because of degradation in the UARS power system, the instruments on board are now operated in a time-sharing mode). Radiance measurements from channels 1-2 and 14-15 are not shown here because these channels are not fully saturated at high latitudes with the 18-km-limb-tracking mode and pointing variations may contaminate the radiance variances.

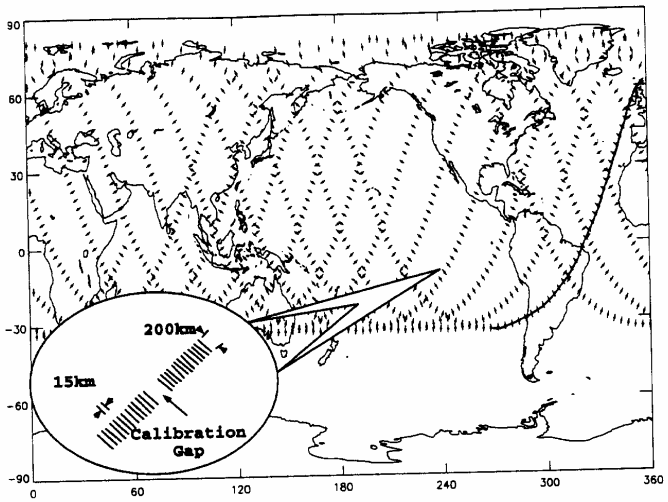

Figure 2. UARS/MLS sampling tracks on 28 December 1994 marked by the first measurement of each major frame (65.5 seconds). The inset details the set of individual measurements in a single major frame with the short lines indicating the orientation of the temperature weighting functions (see text). On this day MLS was preferentially observing the Northern Hemisphere. The ascending portion of orbits 1 is highlighted with solid lines.

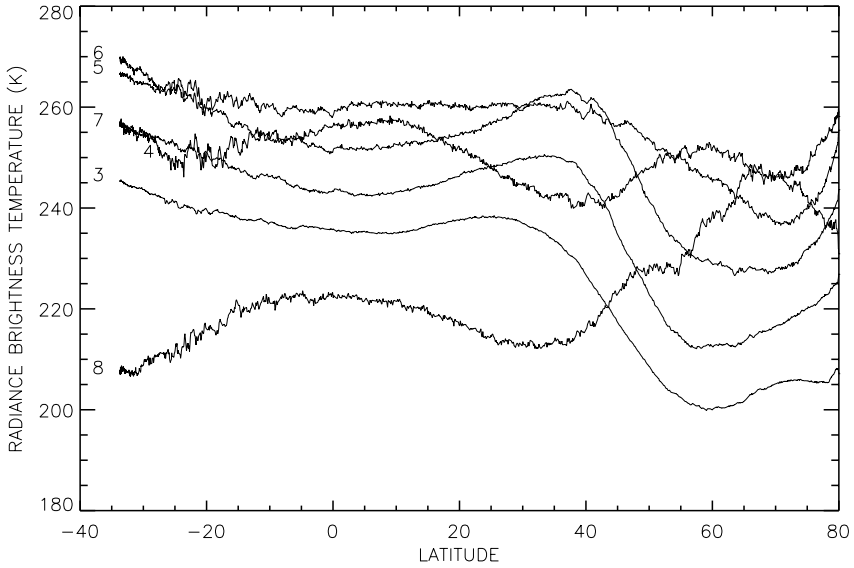

Figure 3. Channel 3-8 radiance measurements from the ascending part of orbit 1 on 28 December 1994.

Figure 3 gives an example of limb-tracking radiance measurements taken on 28 December 1994, when the radiance brightness temperatures observed have large gradients

near the vortex edge (~40-50°N) for channels 3-5. The weaker latitudinal gradients in channel 6-8 radiances suggest that the vortex is weakening at altitudes above 50 km. The radiance gradient differs from orbit to orbit because the vortex was not zonally symmetric at that time in the Northern Hemisphere. Coherent variations can be seen in the radiance fluctuations at different channels (or altitudes) with scales from hundreds to thousands of kilometers. Caution should be given to the interpretation of large-scale radiance variations from channels 7-8. These channels and channel 9 (not shown in Figure 3), close to the O_2 line center, can vary by 3-8 K due to the Zeeman effect associated with Earth's magnetic field. However, these variations generally change slowly along the orbital track except above 70°N and below 25°S (during this observing day) where the viewing angle changes rapidly with respect to the magnetic field lines.

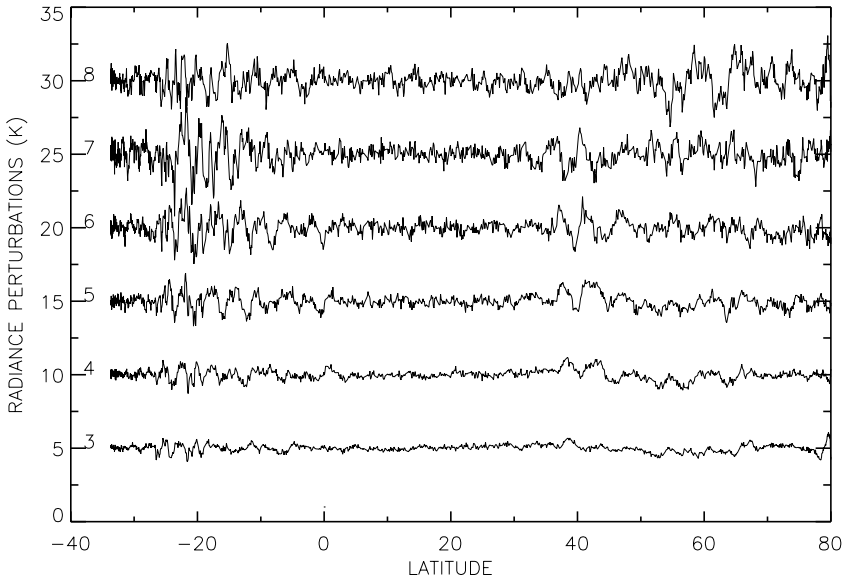

Figure 4. Radiance fluctuations derived from Figure 3 with large-scale (>1000 km) variations removed. Radiance fluctuations of each channel are displaced by 5 K with the channel number indicated at the left of each measurement series. There are more samples near the turning latitudes at 34°S and 80°N than elsewhere. In the middle portion of the orbit, a 10° latitude band corresponds to a distance of ~1300 km.

The small-scale fluctuations can be seen more readily in Figure 4 where large-scale (>1000 km) variations are removed from the radiances in Figure 3. The filtered data in Figure 4 are obtained by differencing the raw and smoothed data (i.e., averages over ~1000 km). The radiance fluctuations from the first ascending orbit show a magnitude of 0.5-3 K at 10°-30°S over South America where deep convection is known to be strong during this period. Oscillations of 1-2K are apparent in the mid- and high-latitude Northern Hemisphere. Phase coherence and amplitude growth with height are clearly seen at some latitudes, suggesting the presence of vertically propagating waves. The 0-30°N region is relatively quiet where the fluctuations are mainly instrument noise.

It should be noted that the MLS radiance fluctuations are expected to largely underestimate atmospheric temperature variations mainly because of the broad vertical and horizontal weighting functions. Atmospheric temperature variances are typically 1-5 K^2 in the

lower stratosphere according to radiosonde measurements [Allen and Vincent, 1995] and 1-10 K^2 in the upper stratosphere from rocket observations [Hirota, 1984; Eckermann et al., 1994]. Moreover, the gravity wave spectra can vary largely with time, height, and place, which adds complexity to interpretation of the radiance fluctuations. The observed magnitude of the radiance fluctuations is a result of convolutions of wave spectra, wave propagating directions, instrument weighting functions, and sampling patterns. Aliasing between wave amplitudes and propagating directions may give problems in directly relating the radiance fluctuations to GW parameters. The quantitative GW information in the MLS measurements is therefore to some extent as limited as what can be obtained from other techniques. Before we further discuss the radiance fluctuations, the weighting functions and the instrument spatial resolution need to be described.

3. Temperature Weighting Functions

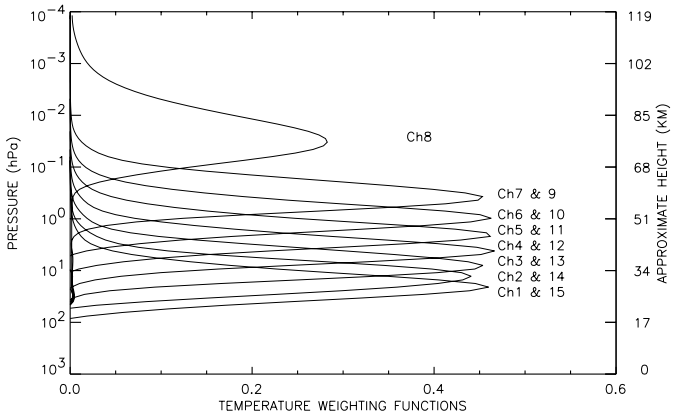

Table 1. The 63 GHz channel parameters

Ch.	Apprx. Height (km)	Layer Thickness (km)	Noise (K)	Elevation Angle (degree)
1, 15	28	10	0.07	3.2
2, 14	33	10	0.08	3.9
3, 13	38	10	0.12	4.5
4, 12	43	10	0.18	5.1
5, 11	48	10	0.26	5.6
6, 10	53	10	0.37	6.0
7, 9	61	10	0.49	6.7
8	80	15	0.45	8.0

Figure 5 Temperature weighting functions of channels 1-15 for the MLS 63 GHz radiometer viewing the limb at 18 km (calculated by W. G. Read).

Instrument spatial resolution and sampling patterns are key to sensing GW-scale disturbances in the atmosphere. The MLS has temperature weighting functions and sampling schemes that are suitable for observing some small-scale gravity waves. Figure 5 describes the MLS temperature weighting functions for 18 km tangent height radiances, showing eight altitude layers (~10-15 km) where temperature is measured by the saturated radiances of different channels. Because the MLS line-of-sight (LOS) direction is perpendicular to the orbit velocity, horizontal averagings are ~100-300 km cross-track (perpendicular to suborbit path) due to radiative transfer through the limb path, and ~30 km along-track (parallel to suborbit path) due to the antenna field-of-view (FOV) smearing. The vertical and horizontal averagings can substantially reduce the magnitudes observed from actual atmospheric temperature fluctuations, but they are still detectable due to low radiometer noise (varying from 0.07 to 0.5 K). Table 1 summarizes the key parameters of the temperature weighting functions and the 63 GHz channel noise.

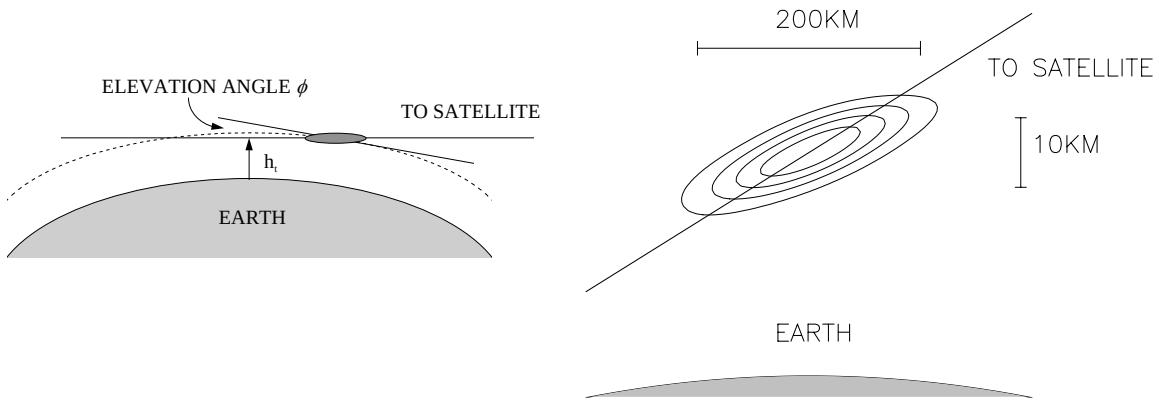

Figure 6 (a) Observing geometry for MLS saturated radiances. (b) Detailed weighting functions in the saturation region where the line of sight is indicated by the straight line. The weighting function in (b), normalized by its peak, is contoured at 0.2, 0.4, 0.6 and 0.8 from edge to center, while the line of sight is indicated by the straight line.

One must consider the 3-dimensional nature of the temperature weighting functions in order to understand what waves can be observed with MLS. Atmospheric waves propagate vertically as well as horizontally, and therefore the amplitude of observed radiance fluctuations depends on orientations of the weighting function relative to wave propagation direction. Figure 6 illustrates the MLS observing geometry where the temperature weighting function has an asymmetric shape in the vertical plane, showing slight tilting from the local horizontal plane. Because of the spatial asymmetry of the temperature weighting functions, the magnitude of radiance fluctuations observed depends on the angle between the LOS direction and wave vector. The observed magnitude is larger if the LOS direction is aligned more along with wavefronts.

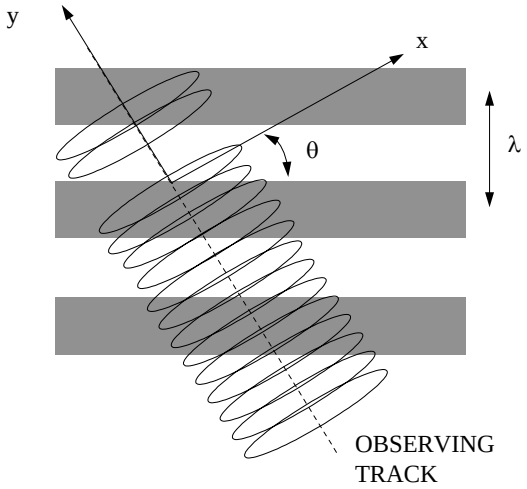

Figure 7. Temperature weighting functions of the saturated radiances projected on the horizontal plane. The footprints of the weighting function move across wavefronts (shaded) with an angle θ, and $k = 2\pi\lambda$.

The horizontal projection of the weighting functions is also asymmetric with a width of ~20 km and a length 150-300 km. As illustrated in Figure 7, the instrument is more sensitive to the waves propagating in the *y* (along-track) direction due to larger averaging in the *x* (LOS) direction: waves are filtered differently in the *x* and *y* directions. As shown in Figure 8 the response to horizontal wavenumber in the *x*-direction (k_x) is cut off at high positive numbers because of the long (~200 km) weighting function. Little responses at small and negative wavenumbers are due to the angle preference of the tilted weighting function which produces severe averaging on the waves with wavefronts not parallel to the LOS direction. The response cutoff at small wavenumbers in the *y*-direction (k_y) is due to the data point truncation that any analysis method must include. The low response for high k_x is caused by the spatial smearing (~15 km) during the 2-second integration and the width of the temperature weighting function (~20 km).

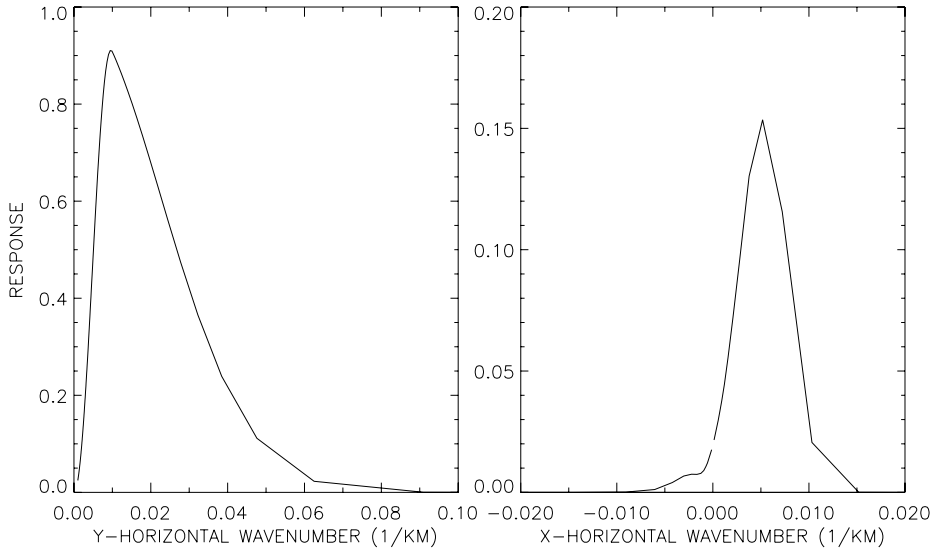

(a) (b)

Figure 8. Radiance responses to the horizontal wavenumbers (a) along and (b) cross the track. The response function in (a) is a simple convolution of a 6-point (~90 km) truncation functions and along-track smearing, while the response function (b) is calculated by convolving the instrument weighting function (Figure 6b) with a 1 K monochromatic wave that has a 10 km vertical wavelength. For a given vertical wavelength, positively propagating waves have wavefronts more parallel to the MLS field of view direction.

The combination of the spectral filters in the *x* and *y* directions yields an optimal viewing angle and an optimal wavelength for MLS to observe atmospheric waves. This is simply because the response functions in Figure 8 provide spectral constraints in two orthogonal directions. The two orthogonal wavenumbers are related by $k_x = k\cos\theta$ and $k_y = k\sin\theta$, where *k* and θ are defined in Figure 7. Figure 9(a) shows the calculated radiance response as a function of horizontal wavelength and observing angle. For waves with a 10 km vertical wavelength, the optimal observing angle is ~30° between the instrument FOV and wavefronts, while the most observable horizontal wavelength is ~100 km. Because the UARS orbit has an inclination of 57°, the MLS is more sensitive to meridionally-propagating waves

near the equator and more sensitive to zonally-propagating waves near the orbit turning latitudes (Figure 2). Figure 9(b) gives the maximal radiance response as a function of vertical wavelength, where poorer sensitivity in smaller vertical wavelengths is the direct effect of the MLS broad vertical weighting functions. There should be a vertical wavelength that is most observable if the GW spectrum and dispersion relation are considered. However, the wave spectrum and its climatology are not well known at present, although some theoretical and observational studies suggest that short vertical wavelengths (<10 km) may dominate the waves in the lower atmosphere (< ~50 km) while long (>10 km) waves, due to atmospheric filtering, are more important in the upper atmosphere [Meek et al. 1985; Smith et al. 1985].

The minimal observable wavelength can be determined from Figure 9 if the minimal detectable radiance amplitude or variance is specified, which depends on the analysis method used. Section 4 describes a simple technique of variance analysis for MLS limb-scanning data, with which the minimal observable vertical wavelength is ~7 km in a monthly average. The minimal detectable variance can be shown to depend on the number of data points averaged and the noise level.

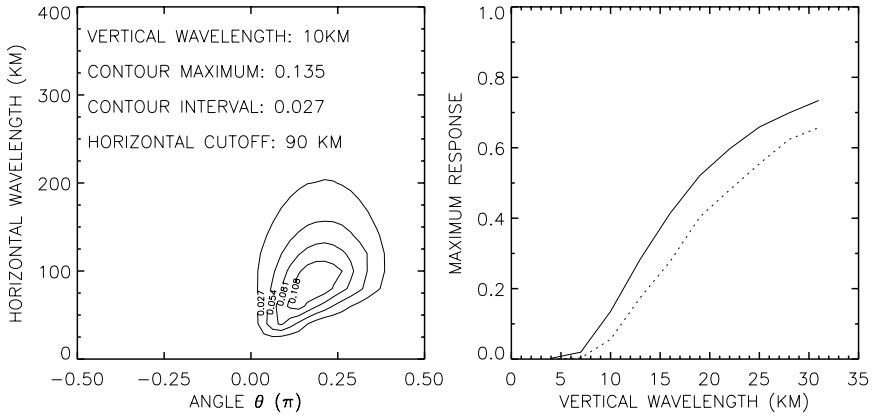

Figure 9. MLS radiance response as a function of (a) horizontal wavelength and observing angle θ and (b) vertical wavelength. The radiance responses in (b) correspond to the peak value in (a), where the solid (dashed) line is for channel 1 (8).

4. Variance Analysis

The method discussed here is a radiance variance analysis that can be used to derive the atmospheric temperature variance from the saturated radiances measured with the MLS limb-scan mode (like one in Figure 1). There is a maximum of 6 consecutive data points in the bottom of each scan where all channels can meet the saturation requirements. A radiance variance for each channel can be calculated from these 6 measurements. The radiance variance calculated for a give channel contains instrument noise and atmospheric temperature

variations from a specified altitude layer as illustrated in Figure 2. To calculate the radiance variance, a linear variation is firstly removed from the 6 radiance measurements, which removes effects of the weak tangent pressure dependence and large-scale wave modulations. Subsequently, the estimated total radiance variance for a given channel, $\tilde{\sigma}^2$, similar to the definition of reduced chi-square, is obtained by

$$\tilde{\sigma}^2 = \frac{1}{4}\sum_{i=1}^{6}(y_i - a - bz_i)^2 \quad (1)$$

where y_i and z_i denote, respectively, radiance measurements and tangent heights. Parameters a and b are determined from the linear least squares fit to the 6 measurements, and 4 is the degree of freedom. As we discussed above, this total radiance variance, σ^2, is mainly due to atmospheric temperature fluctuations, instrument noise and other possible error sources such as non-linear terms in the pressure dependence, namely,

$$\sigma^2 = \sigma_{GW}^2 + \sigma_N^2 + \sigma_{NL}^2 \quad (2)$$

where σ_N^2 is the variance due to instrument noise for the given channel and is known from instrument calibrations in each limb scan. The non-linear pressure contribution, σ_{NL}^2, is small and only important for channels 1/15 and 2/14, and can be reasonably estimated from radiance models (when these channels are used in the analysis). As a result, the atmospheric fluctuation, σ_{GW}^2, can be derived by subtracting σ_N^2 from the estimated total radiance variance $\tilde{\sigma}^2$. We now interpret the atmospheric temperature fluctuations contributing to the radiance variance as a manifestation of upward propagating GWs [Hines 1960]. The same procedure is repeated for all the radiance channels, and the results are averaged for the channel pairs that are symmetric about the line center. Other fluctuation sources, such as the antenna pointing, are either insignificant or very occasional and, therefore, neglected in the analysis here.

The uncertainty in the estimated total radiance variance is the fundamental limit for detecting weak gravity wave signals, and this depends on the number of data points averaged and the instrument noise. To reduce this uncertainty, we generally average measurements over a month for each latitude-longitude grid. The statistical uncertainty of the averaged radiance variance, therefore, is reduced significantly and given by $\left|\tilde{\sigma}^2 - \sigma^2\right| \approx \sqrt{2/m}\sigma^2$, where m is the total number of data averaged within the grid. For example, an 80-variance average will make a wave variance of 10^{-3} K^2 statistically significant in the channel 2 radiances.

5. Gravity Wave Variances

The variance maps presented in this section are 40-day averages for two periods near solstices: January (20 December 1992 - 29 January 1993) and July (18 June to 28 July 1993), centered on UARS yaw days. Figure 10 shows the resulting maps at seven altitudes, and striking features in these maps are large amplitudes associated with the stratospheric polar vortex in the winter hemisphere and subtropical land masses in the summer hemisphere. These features evolve with height and change remarkably above the stratopause.

Background winds are expected to play a major role in determining the GW variance amplitudes observed with MLS. Theoretical studies [Schoeberl and Strobel 1984; Miyahara et al. 1987] show that a strong background wind is a favored condition for GWs to propagate vertically because of the large intrinsic phase speed (i.e. difference between horizontal wave phase speed and the background wind) that prevents the waves from breaking. One may interpret the enhanced variance associated with the stratospheric polar jet as the result of vertically propagating GWs as well. This interpretation is consistent with some aircraft observations in the lower stratosphere [Hartmann et al. 1989], where a positive correlation

was found between small-scale static stability and wind speed. It is the selective filtering effect of the jetstream that acts to reshape the wave spectrum by allowing upstream propagating GWs to grow more efficiently with height than others, and likely causes the variance enhancement observed in the jetstream. However, horizontal finestructures near the vortex can also contribute to the variance observed by MLS, but we cannot quantify this contribution at present. As another result of background wind filtering, the variances in the subtropical summer hemispheres show larger amplitudes at the latitudes (10°S-30°S in January and 10°N-30°N in July) where winds are stronger. The distribution of these summer GW variances is consistent with that of the large-wavenumber momentum flux calculated from the GFDL SKYHI high-resolution general circulation model [Miyahara et al. 1987], both enhanced over Madagascar, Australia, South Pacific and Brazil during January.

The spatial distribution of variances shown in Figure 10 also provide information on gravity wave sources such as tropospheric convection and surface topography. Tropospheric cumulus convection, frequently occurring in the summer over tropical and subtropical land masses, is most likely responsible for the large stratospheric variances observed near Madagascar, North Australia and Brazil during January, and South Asia, Central America and North Africa during July. However, not all convectively-generated GWs can propagate into the stratosphere because of background wind structures. As discussed above, the prevailing subtropical winds may play an important role to allow only some convective disturbances to reach the stratosphere. Topography-related variances can be seen clearly in the maps from channels 8 and 7/9, showing the enhancements over Europe, Asia and America during January and July, and over Andes during July. The zonal asymmetries of the wintertime jetstreams in the stratosphere are generally believed due to differences in surface topography and tropospheric forcings between the two hemispheres, and GWs may provide a considerable contribution to such structures.

The height variation of the normalized variances (Figure 11) reveals some important aspects of the propagating nature of the observed perturbations. Despite very different amplitudes in the lower stratosphere, these variances exhibit approximately the same growth rate with height throughout the stratosphere, which is consistent with the theoretical exponential growth for non-breaking GWs and rocket observations [Hirota and Niki 1985]. This property in variance growth further supports the gravity wave interpretation of the radiance variance observations. Saturation of the normalized variances is observed in the mesosphere, implying wave breakdown/saturation and momentum drag at these altitudes [Fritts 1984]. In Figure 12, zonal means of the normalized variances show that the saturation occurs lower over the vortices (50°N-70°N in January and 50°S-70°S in July) and subtropical land masses (10°S-30°S in January and 10°N-30°N in July). This suggests that the stratospheric jets would be closed at somewhat lower altitudes in these places, consistent with the structure of climatological mean zonal winds during these periods [Fleming et al. 1990]. Moreover, dynamic heating due to the GW breaking/saturation in the jetstreams may reverse the temperature lapse rate remarkably and create temperature inversion layers in the mesosphere. Recent maps of temperature inversions in the mesosphere [Leblanc et al. 1995] show a distribution supported by the MLS wave variance observations.

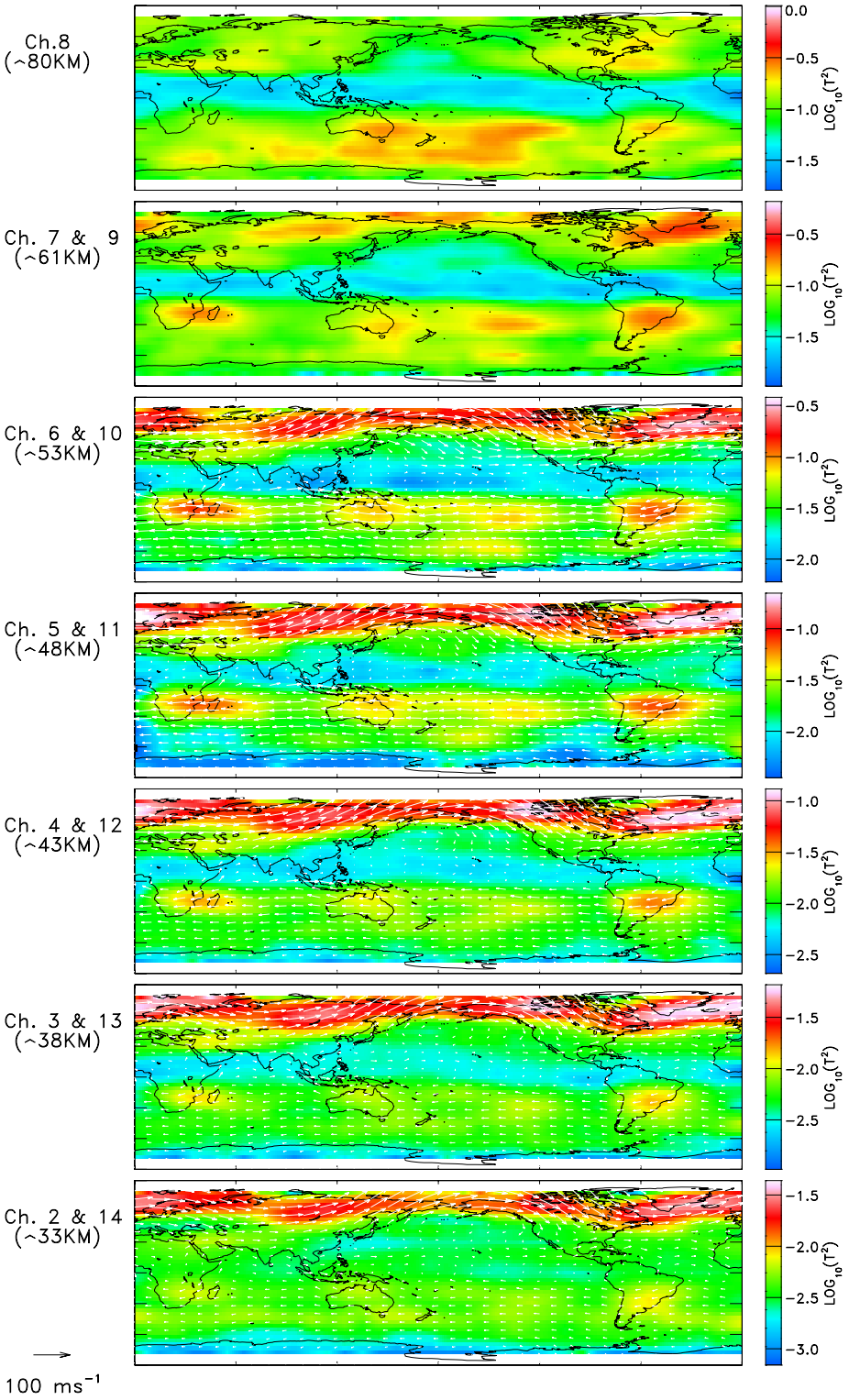

Figure 10(a). Maps of gravity wave variances for January. Latitude and longitude bins are respectively 5° and 10° with more than 40 measurements in each grid point. The variances are in a unit of K^2 and colored in a logarithmic scale, i.e., $\log_{10}(\sigma^2_{GW})$. Winds (up to ~1 hPa) are derived from the US National Meteorological Center data [Manney et al. 1994] and averaged over the same periods.

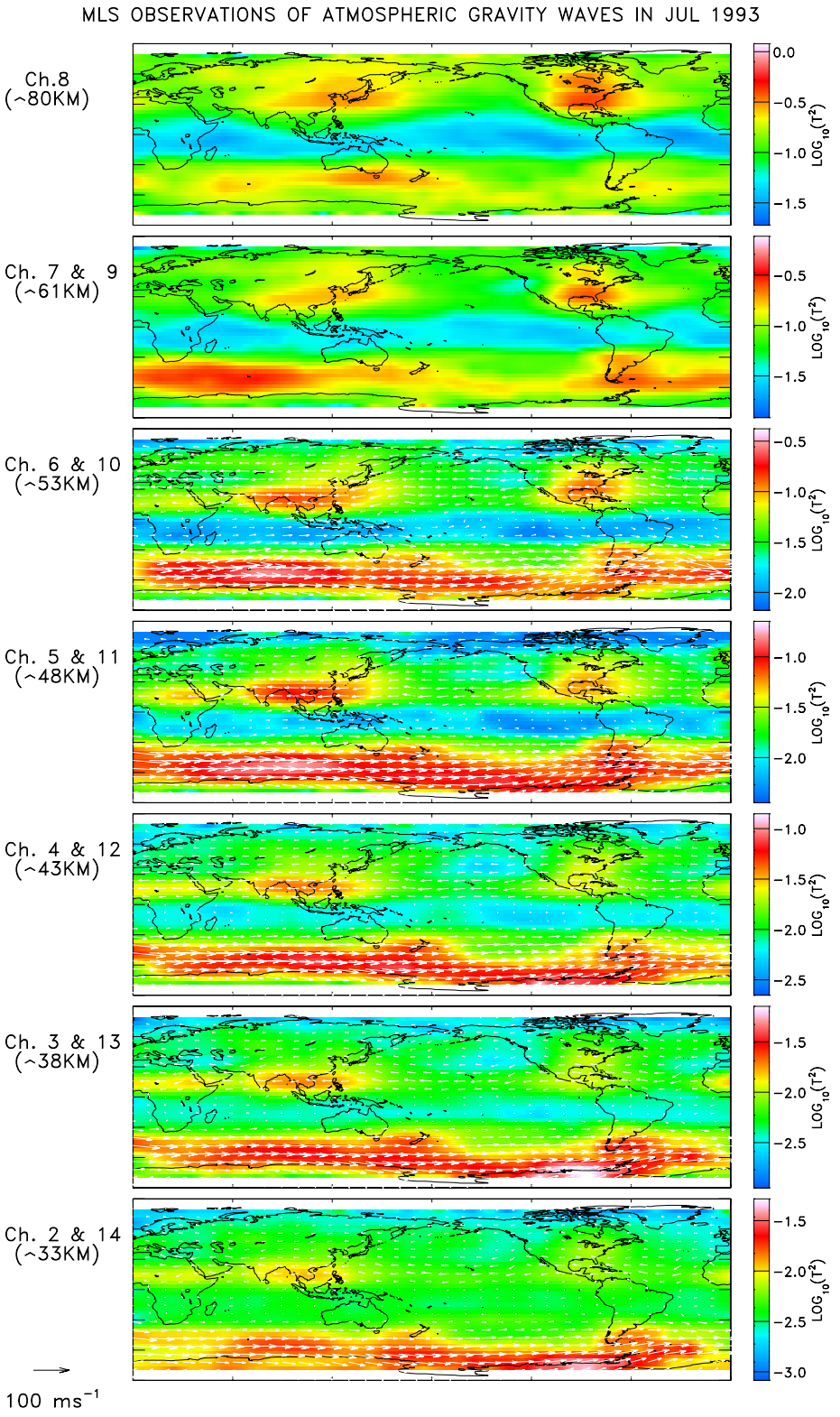

Figure 10(b). As in Figure 10(a) but for July.

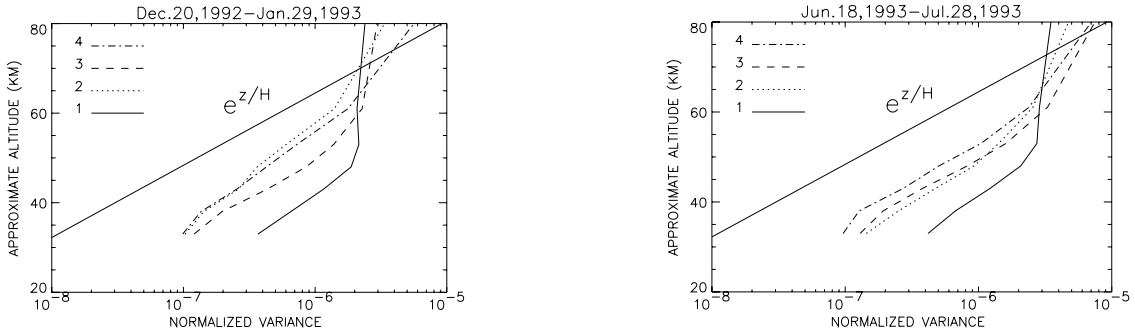

(a) (b)

Figure 11. Variance growth at different latitudes during (a) January and (b) July compared with the exponential growth expected for non-breaking GWs. The variances are normalized by the squared mean radiance brightness temperature.

Alexander and Holton [this volume] have simulated the GW variances that would be observed by MLS, using a quasi-linear model with a broad wave spectrum input at the lower boundary and convolving the predicted temperature variations at higher altitudes with the weighting functions similar to those in Figure 2. In their simulations the GW forcing at the lower boundary was set to be uniform in latitude and longitude, left only with mean zonal winds as variables affecting the wave spectra. As a result, a non-uniform distribution of the temperature variance is obtained and strikingly similar to the variance maps observed by MLS, very much catching the first-order variability. The non-uniform distribution resulted from a uniform forcing again suggest the importance of background winds in gravity wave propagation in the middle atmosphere. It is also suggested by their model calculations that the variances observed by MLS are much likely due to the atmospheric GWs and hence useful for validating some GW parameterization schemes.

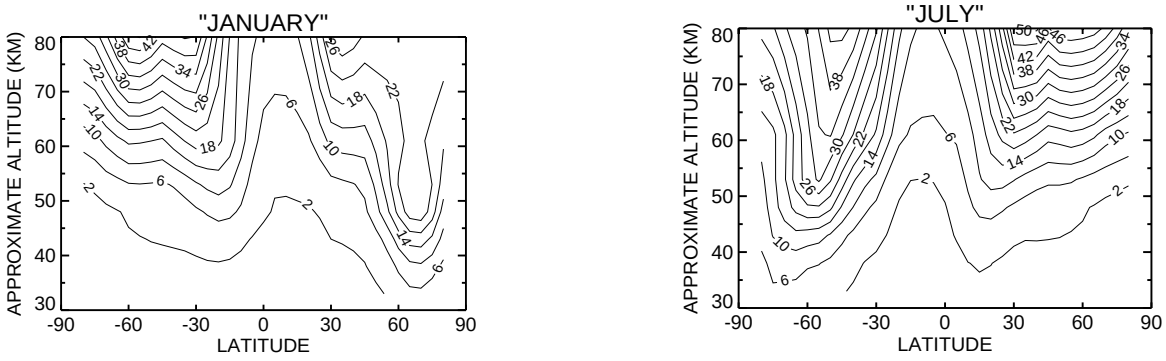

(a) (b)

Figure 12. Zonal mean normalized GW variances for (a) January and (b) July. Contours are in units of 10^{-7}.

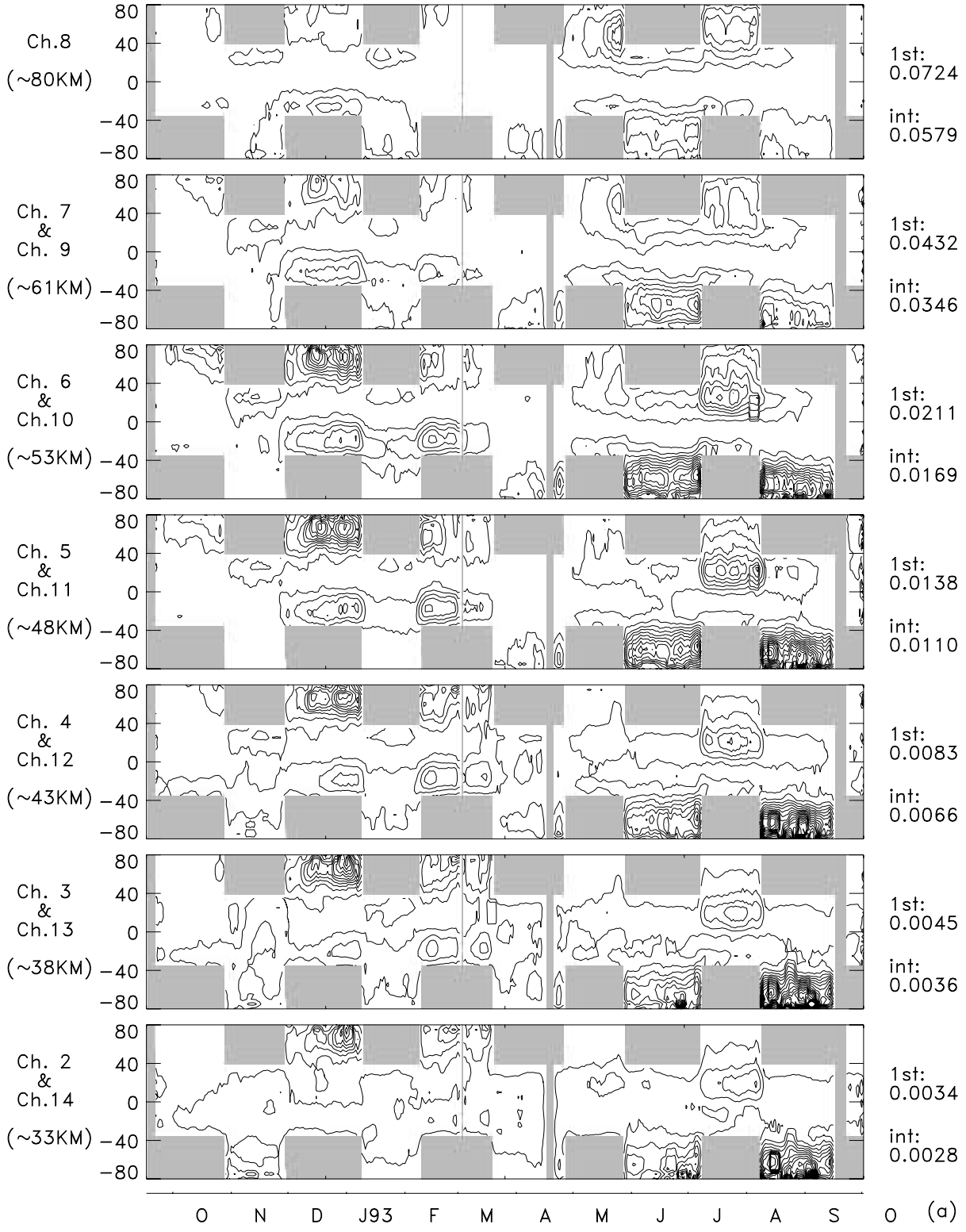

Figure 13(a). Time-latitude plots of daily GW variances for ascending measurements. The first contour and contour interval, in units of K^2, are noted on the right of each panel. A 5-day smoothing is employed for each latitude band with data gaps highlighted by shaded areas. The large data gaps alternated at high latitudes are caused by the UARS yaw maneuvers. At a given latitude the MLS looking angle with respect to the atmosphere is approximately the same for an entire UARS month.

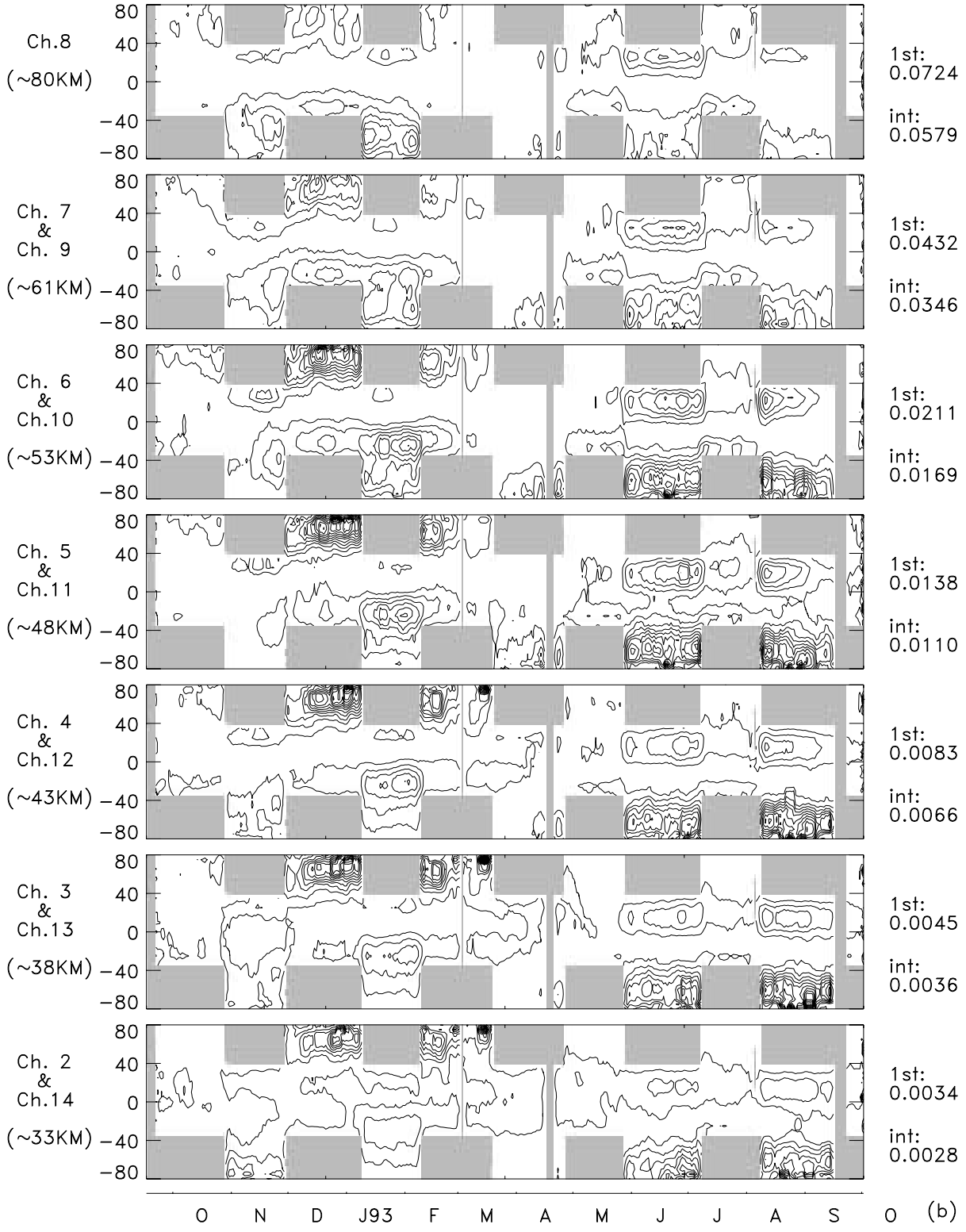

Figure 13(b). As in Figure 13(a) but for descending measurements.. As a result of the yaw maneuver, the MLS viewing direction changes at a given latitude, providing an opportunity for observing wave propagation directions. To the first-order approximation, the variance differences between ascending and descending measurements are caused by the angle variations between the instrument FOV and wave vectors.

Figure 13 provides time series of daily averaged wave variances for the period of October 1992-October 1993. Ascending-descending differences are evident in the averaged wave variances, implying complicated propagation behaviors of the GWs. Let us focus on the features in the 0-40° latitude summer hemisphere which show a strong annual variation in the stratosphere and a somewhat semiannual variation in the mesosphere. These variances, as discussed above, they are likely associated with the GWs generated by tropospheric deep convection and reach the stratosphere with aid of strong westward winds. During the winter/summer months the variances in the stratosphere are very sensitive to the MLS viewing geometry, showing a large difference before and after the yaw days. Since the variances generally vary slowly with time within a UARS month (i.e., the time period between two adjacent yaw maneuvers) for both ascending and descending orbits, the sudden decreases/increases in the variances after a yaw maneuver are due to the changes of MLS viewing geometry with respect to propagating GWs.

The scenario at these latitudes needs to be that the GWs propagate eastward in opposite of background winds in order to explain all variance differences observed from the ascending and descending measure-ments [Figure 14]. As shown in the early analysis [Figures 8-9], the convolution of the temperature weighting functions with an eastward propagating GW can generate large differences in the observed variances with different viewing angles. These observations are consistent with the expectations from the simple gravity wave propagation theory [Lindzen, 1981] and the simulations in a more realistic atmosphere [Alexander and Holton, this volume]. It can be also noted in Figure 13 that the pattern of ascending-descending differences changes with height, suggesting that the wave propagation directions are functions of altitude as well as latitude.

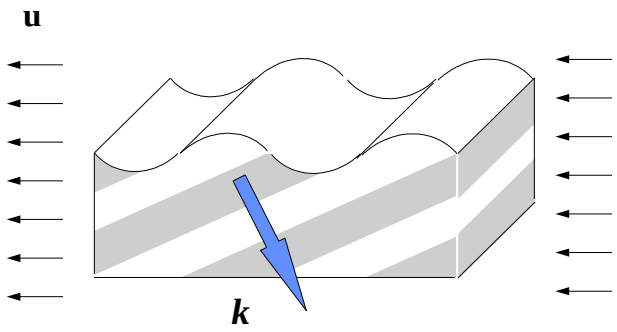

Figure 14. Gravity wave propagation in a background wind, as suggested by the MLS wave variance observations, showing the zonal wave vector k_λ in opposite of the wind velocity **u**.

6. Summary and Conclusions

The radiance fluctuations due to atmospheric GWs have been considered as "noise" to the MLS retrieval, in fact, to most remote sensing techniques. This "noise" is reflected in the Chi-square analysis or error budget analysis of desired products [i.e., Fishbein et al. 1996; Fetzer and Gille 1994]. However, this paper shows that the atmospheric temperature variances can be extracted from the total radiance variances with accurate and frequent on-board calibration, and therefore provide useful information on small-scale wave variability in the middle atmosphere.

The MLS maps of GW activity can contribute substantially to our knowledge of gravity wave generation, propagation, and breakdown, which provide an observational basis for refining the parameterization schemes used in atmospheric modelings. The advantage of using satellite measurements for GW studies is their continuous spatial and temporal coverage with one calibration standard. High-resolution MLS limb-tracking and normal limb-scan

observations have clearly shown some detectable wave signals in the saturated radiances. The major results from this new data set are summarized in the followings:

- The MLS 63 GHz channels can measure atmospheric temperature fluctuations of small (~100 km) horizontal and large (>10 km) vertical scales in 30-80 km altitudes. For instance, a variance of 10^{-3} K^2 can be statistically significant in a 10°x5° monthly averaged map for channel 2 and 14 saturated radiances.
- The wave variances calculated from the saturated radiances reveal some interesting new features associated with the stratospheric polar vortices, tropospheric deep convection zones, and surface topography. Much of the observed variance enhancements can be explained with gravity waves propagating in strong background winds.
- The normalized variances show the expected exponential amplitude growth with height in the stratosphere and saturation in the mesosphere.
- The wave variance is dominated by an annual variation in the stratosphere and a semiannual variation in the mesosphere.
- Separate analyses of the ascending and descending measurements show that the variances are sensitive to wave propagation directions, and suggest that the subtropical variances associated with deep convection are likely caused by the gravity waves that propagate upward and eastward in the prevailing westward stratospheric wind.

Further study of this data set will be focused on the gravity wave spectrum and the structures of the strong radiance perturbations in the stratospheric polar vortex. More difficult questions such as, to what extent the vortex finestructures contribute to the MLS radiance variances, and how gravity and planetary waves interact with each other, need to be answered. The limb-tracking data are particularly useful for addressing these questions and need to be fully explored in the future. More advances in the GW observations are anticipated while the UARS MLS continues collecting data with the limb-tracking mode.

The technique described in section 4 for variance analysis is for general purposes and can be used for measurements from the MLS 183 GHz channels as well. Similar to the 63 GHz radiometer, the 183 GHz radiances will saturate to the atmospheric temperature of various altitude layers. The differences, however, are their temperature weighting functions and a narrower beamwidth for the 183 GHz channels. These differences allow us to compare the variances calculated from the two radiometers so as to gain more knowledge about the height variation of temperature fluctuations.

Acknowledgments. We thank Joan Alexander, Bill Read, Evan Fishbein, Jim Holton, Gloria Manney and Lee Elson for valuable discussions, and Robert Jarnot, Dennis Flower and Richard Lay for operating the instrument. This work was performed at the Jet Propulsion Laboratory, California Institute of Technology, under contract with the National Aeronautics and Space Administration.

References

Alexander, M. J., and J. R. Holton (1996), Non-stationary gravity wave forcing of the stratospheric zonal mean wind. *This volume.*

Allen, S. J., and R. A. Vincent (1995), Gravity wave activity in the lower atmosphere: Seasonal and latitudinal variations. *J. Geophys. Res.*, **100**, 1327-1350.

Barath, F.T., et al. (1993), The Upper Atmosphere Research Satellite Microwave Limb Sounder instrument, *J. Geophys. Res*. **98**, 10,751-10,762.

Eckermann, S., I. Hirota, and W. K. Hocking (1994), Gravity wave and equatorial wave morphology of the stratosphere derived from long-term rocket soundings, *Q. J. R. Meterol. Soc.*, 121, 149-185.

Fetzer, E.J., and J.C. Gille (1994), Gravity wave variance in LIMS temperatures. Part I: Variability and comparison with background winds. *J. Atmos. Sci.*, **51**, 2461-2483.

Fishbein, E. F., R.E. Cofield, L. Froidevaux, R.F. Jarnot, T. Lungu, W.G. Read, Z. Shippony, J.W. Waters, I.S. McDermid (1996), Validation of UARS MLS temperature and pressure measurements, *J. Geophys. Res.*, **101**, 9983-10,016.

Fleming, E. L., S. Chandra, J. J. Barnett, and M. Corney (1990), Zonal mean temperature, pressure, zonal wind and geopotential height as functions of latitudes. *Adv. Space Res.*, 10, 11-59.

Fritts, D.C. (1984), Gravity wave saturation in the middle atmosphere: A review of theory and observations. *Rev. Geophys.*, 22, 275-308.

Fukao, S., M.D. Yamanaka, N. Ao, W.K. Hocking, T. Sato, M. Yamamoto, T. Nakamura, T. Tsuda, and S. Kato (1994), Seasonal variability of vertical eddy diffusivity in the middle atmosphere, 1. three-year observations by the middle and upper atmosphere radar. *J. Geophys. Res.*, **99**, 18,973-18,987.

Hartmann, D. L., K. R. Chan, B. L. Gary, M. R. Schoeberl, P. A. Newman, R. L. Martin, M. Loewenstein, J. R. Podolske, and S. E. Strahan (1989), Potential vorticity and mixing in the south polar vortex during spring. *J. Geophys. Res.*, **94**, 11,625-11,640.

Hines, C. O. (1960), Internal gravity waves at ionospheric heights. *Can. J. Phys.*, **38**, 1441-1481.

Hirota, I. (1984), Climatology of gravity waves in the middle atmosphere. *J. Atmos. Terr. Phys.*, **46**, 767-773.

Hirota, I., and T. Niki (1985), A statistical study of inertia-gravity waves in the middle atmosphere. *J. Meteor. Soc. Japan*, **63**, 1055-1066.

Leblanc, T., A. Hauchecorne, M.-L. Chanin, C. D. Rodgers, F. W. Taylor, and N. J. Livesey (1995), Mesospheric temperature inversions as seen by ISAMS in December 1991. *Geophys. Res. Lett.*, **22**, 1485-1488.

Manney, G. L., R. W. Zurek, M. E. Gelman, A. J. Miller and R. Nagatani (1994), The anomalous Arctic lower stratospheric polar vortex of 1992-1993. *Geophys. Res. Lett.*, **21**, 2405-2408.

Meek, C. E., I. M. Reid, and A. H. Mason (1985), Observations of mesospheric wind velocities 2. Cross sections of power spectral density for 48-8 hours, 8-1 hours, and 1 hour to 10 min over 60-110 km for 1981. *Radio Sci.*, **20**, 1383-1402.

Miyahara, S., Y. Hayashi and J. D. Mahlman (1987), Interactions between gravity waves and planetary-scale flow simulated by the GFDL SKYHI general circulation model. *J. Atmos. Sci.*, **43,** 1844-1861.

Smith, S. A., D. C. Fritts, and T. E. VanZandt (1985), Comparison of mesospheric wind spectra with a gravity wave model. *Radio Sci.*, **20**, 1331-1338.

Schoeberl, M. R., and D. F. Strobel (1984), Nonzonal gravity wave breaking in the winter mesosphere. *Dynamics of the Middle Atmosphere*, J.R. Holton and T. Matsuno, Eds. (Terra, Tokyo, 1984), pp.45-64.

Vincent, R.A., and D.C. Fritts (1987), A climatology of gravity wave motions in the mesopause region at Adelaide, Australia. *J. Atmos. Sci.*, **44**, 748-760.

Waters, J. W. (1993), Chap.8 in *Atmospheric Remote Sensing Microwave Radiometry*, M.A. Janssen, Ed., Wiley, New York, pp.383-496.

Wilson, R., M.L. Chanin, and A. Hauchecorne (1991), Gravity waves in the middle atmosphere observed by Rayleigh Lidar: 2. Climatology. *J. Geophys. Res.*, **96**, 5169-5183.

Wu, D. L. and J. W. Waters (1996), Satellite observations of atmospheric gravity waves, *J. Res. Lett*., in press.